MATERIALS CHEMISTRY FRONTIERS

RESEARCH ARTICLE

View Article Online
View Journal | View Issue



Cite this: *Mater. Chem. Front.*, 2025, **9**, 1181

# Conformational regulation to realize modifiable ESIPT (excited-state intramolecular proton transfer) through intermolecular interactions†

Shao-Zhe Yi,[a] Bao-Ning Li,[b] Wen He[a] and Mei Pan *[a]

Received 9th January 2025,
Accepted 13th February 2025

DOI: 10.1039/d5qm00012b

rsc.li/frontiers-materials

Regulating molecular conformation changes is crucial yet challenging for manipulating multiple-responsive emissions in excited-state intramolecular proton transfer (ESIPT) materials. In this work, we explored the specific emission regulation of a dual-ESIPT-active molecule, BDIBD (2,5-bis(4,5-diphenyl-1*H*-imidazol-2-yl)benzene-1,4-diol), by subtly controlling the ground and excited states through different crystallization conformations. Notably, the crystals obtained in dimethylformamide (BDIBD–DMF) and methanol (BDIBD–MeOH) exhibited a single emission band, corresponding to the green and red emission from the keto$^{1st}$ and keto$^{2nd}$ excited states, respectively, while the crystals obtained in acetone (BDIBD–ACE) displayed dual emissions from both states, resulting in an overall yellow color. A comprehensive theoretical study verified that the modified intermolecular interactions, due to different crystallization conformations, regulated emissions by affecting the energy barrier of dual-ESIPT processes. The above results provide a concrete understanding of the regulation of excited-state emissions through ground-state conformational changes in ESIPT processes, as well as unique insights into the design and application of novel ESIPT emission materials.

## 1. Introduction

Organic ESIPT materials in the solid state have been attracting increasing attention owing to their wide applications in many fields, such as optical sensing, laser gain, light-emitting diodes, and anti-counterfeiting materials.[1–7] The ESIPT process involves an intrinsic four-level photocycle (E → E* → K* → K → E).[8] Upon absorption of light, a fast tautomerization process occurs, leading to either the sole emission of the tautomer or multiple emissions if a balance exists between the E* and K* states.[2,9] This usually results in large Stokes shifts, sensitive external environmental responsiveness and minimal reabsorption.[9–11] Besides, this unique photoinduced keto–enol tautomerism leads to a complex transient chemical change from the E to K tautomer, enabling the realization of a regulatable luminescence mechanism.[12–14] To achieve a broader photoluminescent range, enriched photophysical phenomena, and multi-stimulus optical responses, the incorporation of multiple ESIPT sites into a single molecule is an effective strategy.[15,16] Meanwhile, rich controllable sites provide a good platform for emission regulation.[17] However, it is also a daunting task to concretely understand the regulation mechanism of excited-state emissions in molecules with dual or multi-ESIPT sites due to the more complicated processes. These processes include not only the modulation of the enol–keto tautomeric transition but also the transitions between the keto$^{1st}$ and keto$^{2nd}$ succeeding excited states.

So far, most research on the ESIPT mechanism has focused on materials in solution systems.[18–22] A classic example is the work by Pi–Tai Chou *et al.*, who used the ESIPT-active molecule 7-hydroxy-1-indanone as a prototype to design ESIPT chromophores by fusing benzene and naphthalene rings.[23] By carefully controlling the balance between the destruction of aromaticity and the compensation of π-conjugation, they obtained three materials with different proton transfer driving forces in solution. Another common approach is adjusting the strength of hydrogen bonds to regulate the balance between enol and keto emission.[4,24–26] For example, Dongwhan Lee *et al.* reported an ESIPT polymer with white light emission in solution, which is regulated by the introduction of electron-donating/-withdrawing substituents.[27] However, to better mimic the more complicated natural systems and explore new luminescence mechanisms, the study of materials in the solid-state crystalline

[a] *MOE Laboratory of Bioinorganic and Synthetic Chemistry, Lehn Institute of Functional Materials, IGCME, GBRCE for Functional Molecular Engineering, School of Chemistry, Sun Yat-Sen University, Guangzhou 510006, China. E-mail: panm@mail.sysu.edu.cn*

[b] *School of Chemistry and Chemical Engineering, Yulin University, Yulin 719000, China*

† Electronic supplementary information (ESI) available: All experimental and characterisation data, as well as photophysical and NMR spectra. See DOI: https://doi.org/10.1039/d5qm00012b

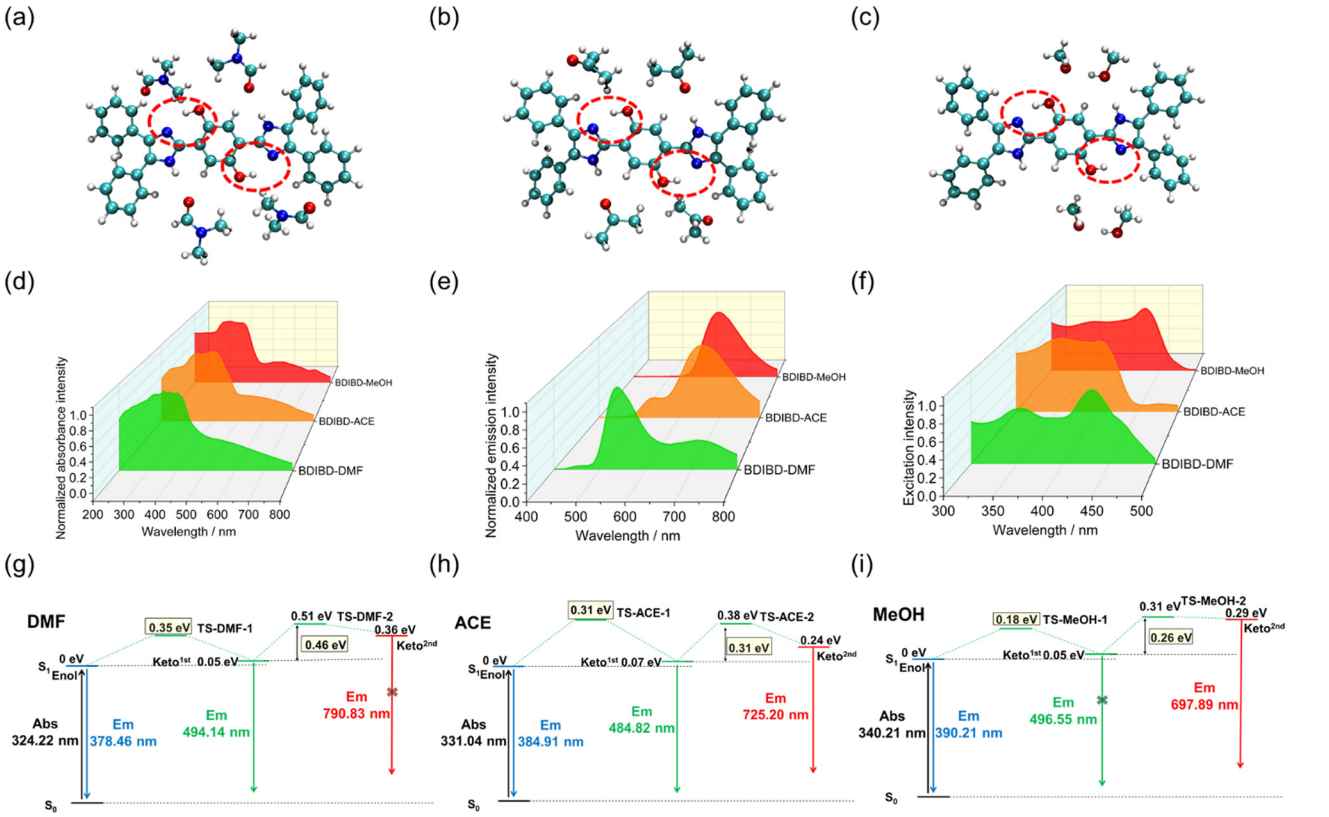


Fig. 1 Chemical structures and proton transfer sites of (a) BDIBD–DMF, (b) BDIBD–ACE and (c) BDIBD–MeOH. Normalized (d) absorbance spectrum, (e) emission spectrum, and (f) excitation spectrum of the crystals in the solid state. ONIOM-EE (TD-M06-2X/6-31G (d,p):UFF)-calculated dual-ESIPT mechanism with relative electronic energy (eV) and wavelength (nm) for (g) BDIBD–DMF, (h) BDIBD–ACE, and (i) BDIBD–MeOH.

state is more informative. Notably, solid fluorescent sensors have obvious advantages in reusability and portability, and drawbacks such as concentration problem can be ignored.[1,28–30] While many different chromophores have been used for ESIPT emission, the design of new ESIPT regulation strategies for solid materials, especially organic molecules, is still challenging.[4,31–33] Cleverly regulating intermolecular interactions is an ideal strategy as it can regulate the emissions by tuning the energy barrier of dual-ESIPT procedures. In order to clarify the ESIPT mechanisms of virtually identical materials that differ only in the strength of intermolecular interactions, a deeper exploration from both experimental and theoretical perspectives is needed.

Herein, three crystals from different solvents based on the same molecule, BDIBD (2,5-bis(4,5-diphenyl-1*H*-imidazol-2-yl)benzene-1,4-diol), were synthesized and studied to reveal the above considerations (Fig. 1 and Fig. S1–S3, Tables S1–S4, ESI†). It is interesting to find that the crystals obtained in DMF (BDIBD–DMF) and MeOH (BDIBD–MeOH) exhibit single emission bands, which separately correspond to keto$^{1st}$ and keto$^{2nd}$ emission, while crystals obtained in acetone (BDIBD–ACE) display both of them. A detailed study reveals that the regulation of intermolecular interactions in different ground-state crystallization conformations drives the various emissions, as revealed by steady-state luminescence studies, density functional theory (DFT) and time-dependent density functional theory (TD-DFT) calculations. Besides, theoretical results prove that the keto$^{1st}$ and keto$^{2nd}$ excited states in molecules with different crystalline conformations and intermolecular interactions have different proton-transfer ability, leading to modifiable ESIPT procedures and emissions. Overall, the experimental and computational results together confirm the unique intermolecular interaction mechanism.

## 2. Results and discussion

ESIPT-active molecule BDIBD was previously reported, which can undergo a two-step ESIPT process, giving enol, keto$^{1st}$ and keto$^{2nd}$ forms of luminescence. Through recrystallization in DMF/MeOH (v/v 1/10), acetone and MeOH, three crystals named BDIBD–DMF, BDIBD–ACE, and BDIBD–MeOH, respectively, were synthesized. The designed crystals were structurally characterized by X-ray single crystal diffraction analysis. Detailed structural information and packing diagrams of all the chromophores were obtained (Fig. 1a–c and Fig. S1–S4, Tables S1–S4, ESI†). The formula of the compounds is $C_{21}H_{20}N_3O_2$ (solvent *N*,*N*-dimethylformamide and BDIBD with a ratio of 2 : 1), $C_{21}H_{19}O_2N_2$ (solvent acetone and BDIBD with a ratio of 2 : 1), and $C_{39}H_{38}N_4O_5$ (solvent methanol and BDIBD with a ratio of 3 : 1). Significantly, BDIBD–DMF and BDIBD–ACE are isomorphic, which crystallize in the monoclinic *C*2/*c* space group. BDIBD–MeOH crystallizes in a tighter lattice, which is the triclinic $P\bar{1}$ space group.

 

As shown in Fig. 1 and Tables S1–S4 (ESI†), all the BDIBD molecules in the crystals have similar molecular conformations with similar bond lengths and angles and approximate dihedral angles between the benzene ring and imidazole ring units. In contrast, from BDIBD–DMF to BDIBD–ACE and then to BDIBD–MeOH, the torsion angle between the benzene ring and the imidazole ring decreases slightly, while the molecular conjugation increases gradually, leading to emission at longer wavelengths. However, overall, the conformational change of the molecule is minimal. It is considered that the conformation difference of BDIBD molecules in the crystals is not the main reason for different FL properties. Thus, we focused on the influences of intermolecular interactions in the crystals. The crystal structures of the molecules support their different luminescent attributes, as will be discussed below.

BDIBD–DMF was reported in our previous study. The structure of BDIBD–ACE has cell parameters of $a$ = 34.052(3) Å, $b$ = 5.8249(6) Å, $c$ = 17.732(2) Å, $\alpha = \gamma = 90^\circ$, and $\beta$ = 102.677(10)°. The structure of BDIBD–MeOH has cell parameters of $a$ = 9.7843(9) Å, $b$ = 11.0773(12) Å, $c$ = 15.682(2) Å, $\alpha$ = 99.283(10)°, $\beta$ = 95.760(9)°, and $\gamma$ = 93.226(8)°. The N atom of the imidazole acts as an acceptor of the hydrogen bonds, and –O–H···N inhibits the ESIPT progress. The N···H distance between the hydrogen bonds of –O–H···N is as large as 1.916 Å in BDIBD–DMF. By comparison, the N···H bond distance is 1.880 Å in BDIBD–ACE and 1.820 Å in BDIBD–MeOH, revealing that ESIPT progress is relatively easier in BDIBD–MeOH but harder in BDIBD–DMF (BDIBD–DMF > BDIBD–ACE > BDIBD–MeOH). The O···N distances of the crystals follow a similar pattern, *i.e.*, BDIBD–DMF (2.643 Å) > BDIBD–ACE (2.622 Å) > BDIBD–MeOH (2.566 Å). As shown in Fig. S1–S3 (ESI†), solvent molecules can form intermolecular hydrogen bonds with the oxygen atom in the BDIBD molecule, which competes with intramolecular hydrogen bond formation and inhibits the ESIPT process. This leads to the molecule favoring enol or keto$^{1st}$ emission. The hydrogen bond length between BDIBD and DMF is 2.567 Å, indicating a relatively strong intermolecular interaction that significantly suppresses the ESIPT process. In contrast, the hydrogen bond length between BDIBD and ACE is 2.607 Å, and the suppression of the ESIPT process by the intermolecular H-bond is weaker. The hydrogen bond length between BDIBD and MeOH is only 2.714 Å. In addition, the intermolecular hydrogen bond is relatively parallel to the intramolecular hydrogen bond, leading to a minimal impact on the electron cloud distribution and a weaker competitive effect. Therefore, it tends to form intramolecular hydrogen bonds and undergo the ESIPT progress. Besides, the strength of C–H···π and π–π interactions in BDIBD–ACE is stronger than that in isomorphic BDIBD–DMF, indicating that is BDIBD–ACE packed more tightly and tends to have low-energy emission.

We first explored the photophysical properties of the crystals (Fig. 1d–i and Fig. S5, Tables S5, S6, ESI†). As shown by the distinct powder diffraction patterns of the crystals (Fig. S6, ESI†), the identity of each phase was confirmed. All the crystals exhibit similar absorption bands, which are mainly assigned to the π–π* transition, and few n–π* transitions can possibly take place. Significantly, in the emission spectra of crystals in the solid state, as shown in Fig. 1e, the major emission bands of BDIBD–DMF and BDIBD–MeOH peaked at 530 nm and 650 nm, respectively. In comparison, BDIBD–ACE exhibits two emission bands, which were located at 520 nm and 670 nm. Combining the excitation spectrum, all the emission peaks exhibit large Stokes' shift of > 170 nm, which should be reasonably attributed to keto form emission. Specifically, the emission peaks at ~500 nm should correspond to keto$^{1st}$, and the peaks at ~650 nm should be attributed to keto$^{2nd}$. The photoluminescence quantum yield (PLQY) of the chromophores is similar, with PLQY of 9.1% (BDIBD–DMF), 6.8% (BDIBD–ACE), and 7.8% (BDIBD–MeOH). The luminescence decay lifetimes of the crystals are all sub-nanosecond (~1 ns, Fig. S5, ESI†).

In our study, density functional theory (DFT) was used to optimize the molecular structure in the ground state ($S_0$), while the geometry of the excited states was optimized with time-dependent density functional theory (TD-DFT).[34] To provide different ESIPT mechanisms in the crystals, we used the ONIOM (QM/MM) approach with a two-layer model, combining quantum mechanical (TD)-M06-2X/6-31G (d,p) with universal force field (UFF). The clusters for ONIOM calculations were cut from the X-ray single-crystal structure in the experiment. One BDIBD molecule was placed at the center of the model and treated at the QM level, which was optimized without constraint. The surrounding molecules were computed by low-level UFF force field with QEQ charges and kept frozen during optimizations. High layer was completely surrounded by low layer (Fig. 2a–c). From the chemical structure of BDIBD, we can deduce that there should be two ESIPT-related hydrogen bonds in BDIBD, and thus two proton transfer states may exist. The molecule without proton transfer is labeled as Enol. The molecule with one proton transferred is named Keto$^{1st}$, and the molecule with two protons transferred is called Keto$^{2nd}$. Due to the high Hartree–Fock (HF) contribution (54%), M06-2X tends to slightly overestimate keto$^{2nd}$ energy (Tables S7–S12, ESI†). However, the M06-2X functional offers significant advantages in calculating energy barriers, which is our primary focus, and can accurately account for the weak interactions between solvent molecules and BDIBD. Thus, it was considered the optimal choice for our study.

To explore the light-emitting properties, the emission wavelengths of the three crystals were calculated in the solid phase, as shown in Fig. 1f–i. There is no local minimum for keto-$S_0$, indicating that BDIBD returns to enol-$S_0$ without barrier. For BDIBD–DMF, the calculated emission wavelengths of keto$^{1st}$ from $S_1$ to $S_0$ is 494 nm, which is in good agreement with the emission spectrum. The major emission peaks of BDIBD–ACE and BDIBD–MeOH were calculated at 725 nm and 698 nm, respectively (Fig. 1f–i and Tables S7–S29, ESI†). It was deduced that the emission of BDIBD–DMF should come from keto$^{1st}$, while the ones of BDIBD–ACE and BDIBD–MeOH should come from keto$^{2nd}$.

The CAM-B3LYP, PBE0 and ωB97XD calculations (QM part) of key geometry parameters and relative energies (nm) are shown in Tables S7–S12 (ESI†). The calculated results predict

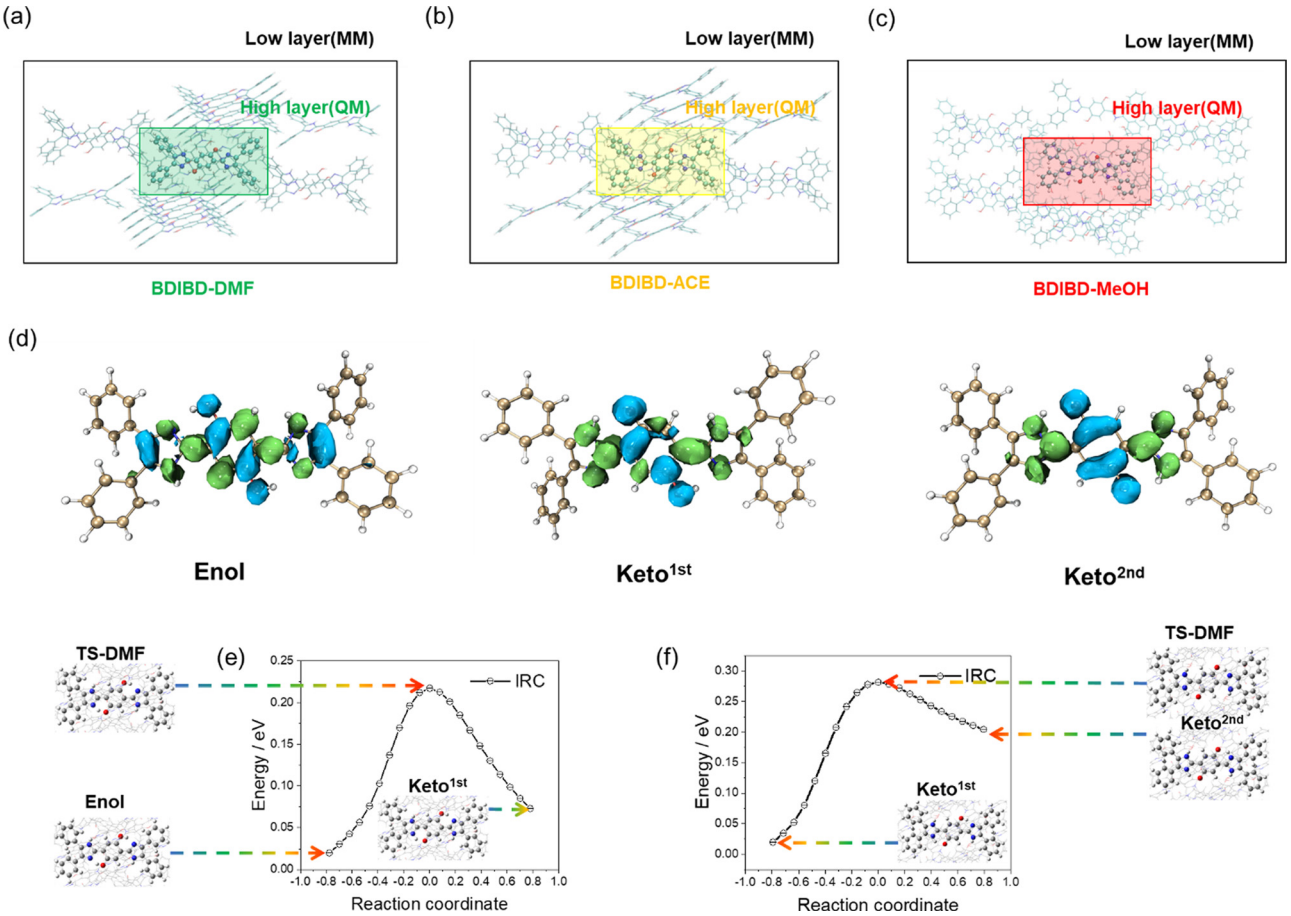


Fig. 2 ONIOM model of (a) BDIBD–DMF, (b) BDIBD–ACE and (c) BDIBD–MeOH. The centered BDIBD is treated as the high layer, and the surrounding molecules are regarded as the low layer. (d) Calculated charge-density difference (CCD) between the $S_0$ and $S_1$ states of the QM part of BDIBD–DMF, with blue and green regions denoting the hole and electron distributions, respectively. Calculated relative energy profile along the excited-state IRC for BDIBD–DMF based on ONIOM-EE (TD-M06-2X/6-31G (d,p):UFF) level: (e) path from enol to keto$^{1st}$, (f) path from keto$^{1st}$ to keto$^{2nd}$.

only slightly lower energies of reactions, and they are very similar to the mainly discussed M06-2X result. All the transitions between $S_0$ and $S_1$ were found to be predominantly HOMO to LUMO with natural bond orbital (NBO) beyond 90% (Fig. S7–S9 and Tables S13–S29, ESI†). In addition, the transition properties of the excited states were analyzed. Since more than one molecular orbital contributes to the excitation of $S_1$, the charge-density difference (CDD) map of the excited states for the three crystals in solid state was analyzed (as shown in Fig. 2d and Fig. S10, S11, ESI†), which was obtained using the Multiwfn[35,36] and VMD[37] package program. It can be seen that the electrons and holes are distributed almost averagely on the phenol and imidazole rings in the three crystals. Based on the electron–hole distribution, it can be concluded that the $S_1$ state of the crystals is a typical locally excited (LE) state.

Moreover, to obtain the exact barrier heights and further clarify the reaction mechanism, we located the TS (transition state) structure of the ESIPT process by adjusting the transferred H proton between O and N atoms. Obviously, on the ground state, the potential energy increases along with the decrease in the N–H bond length, which inhibits the ESIPT progress. It is worth mentioning that all TS structures in the $S_1$ state have only one virtual frequency and that their vibration eigenvectors point towards the correct isomerization reaction orientation. For the $S_1$ state, two TS structures were marked, representing barriers along the paths (Fig. 1g–i). The energy barrier of the first ESIPT progress in BDIBD–DMF is 0.35 eV, which allows ESIPT progress. However, the barrier of the second reaction is 0.46 eV, and the ESIPT reaction is completely prevented.[13,38–44] For BDIBD–ACE, the barriers of the two progresses are similar (0.31 eV); both ESIPT reactions can take place, resulting in keto$^{2nd}$ emission. Besides, a small number of molecules can still return to the ground state in the keto$^{1st}$ form, leading to dual-emission.[13,38–44] The barriers of the two proton transfers are 0.18 eV and 0.26 eV in BDIBD–MeOH, respectively. The ESIPT reaction is very easy to progress, resulting in only keto$^{2nd}$ emission.[13,38–44] In the meantime, we also gain the IRC diagram based on the TS structure, as shown in Fig. 2e, f and Fig. S12, S13 (ESI†). The IRC calculation starts from the given TS structure and calculates the intermediate structure of multiple reaction processes along the reaction path towards two minimal points. Therefore, it can help us intuitively see whether the reactants and products connected by this transition state are the structure

 

we imagine so as to identify that the TS structure is valid and accurate.

A slight variation of the structures will cause a disparity of ESIPT ability. The calculation result shows that the N···H distances between the hydrogen bonds of –O–H···N are 1.878 Å in BDIBD–DMF, 1.756 Å in BDIBD–ACE and 1.679 Å in BDIBD–MeOH (BDIBD–MeOH < BDIBD–ACE < BDIBD–DMF, Tables S30–S39, ESI†) in the excited state. Similarly, the N···O distances are 2.673 Å in BDIBD–DMF, 2.660 Å in BDIBD–ACE and 2.601 Å in BDIBD–MeOH (BDIBD–MeOH < BDIBD–ACE < BDIBD–DMF, Tables S30–S39, ESI†). In addition, the N–H bond distance in the keto form after the ESIPT process is 1.017 Å in BDIBD–DMF, 1.022 Å in BDIBD–ACE and 1.025 Å in BDIBD–MeOH (BDIBD–DMF < BDIBD–ACE < BDIBD–MeOH, Tables S30–S39, ESI†). Compared to BDIBD–DMF, a shorter H-bond shows that the ESIPT progress is relatively easier in BDIBD–ACE and BDIBD–MeOH, revealing the different luminescence for BDIBD in various intermolecular interactions. Mayer bond orders of all bonds were calculated and are shown in Tables S31, S33, S35 and S37 (ESI†). Mayer bond orders can exhibit bonding strength because they have a good correlation with the bond dissociation energy. In general, the larger the Mayer bond orders of a bond, the stronger the bonding strength (Tables S30–S39, ESI†). Results indicate that the bond orders of the hydrogen bonds are 0.1205 in BDIBD–DMF, 0.1328 in BDIBD–ACE and 0.1601 in BDIBD–MeOH (BDIBD–DMF < BDIBD–ACE < BDIBD–MeOH) in the excited state, which is consistent with previous results.

As is well known, infrared (IR) vibrational spectroscopy is a powerful tool for analyzing hydrogen bonding. The simulated results showed that there were no imaginary frequencies in all the IR spectra of the related geometries investigated in this work. Since the potential ESIPT behavior proceeded along O–H···N, we mainly focused on the IR changes of the $S_0$-state and $S_1$-state hydrogen bonding moieties. As shown in Fig. 3 and Fig. S14 (ESI†), we present the simulated IR vibrational frequency of the O–H and N–H stretching vibration modes for the crystals, based on which specific hydrogen bonding interactions could be found. A red shift of the O–H bond in the IR spectrum indicates an increase in hydrogen bond strength, whereas a blue shift suggests a decrease in hydrogen bond strength. We found an obvious red-shift of the IR vibrational frequencies involved in O–H stretching vibration for both the crystals forms from $S_0$ to $S_1$ state. This reflected that O–H···N should be strengthened in the $S_1$ state. For the enol form, the calculation results show that the wavenumbers of O–H vibrations are 3300 $cm^{-1}$ in BDIBD–DMF, 3100 $cm^{-1}$ in BDIBD–ACE, 2900 $cm^{-1}$ in BDIBD–MeOH (BDIBD–MeOH < BDIBD–ACE < BDIBD–DMF, Table S37, ESI†), revealing that ESIPT progress is easy in BDIBD–MeOH compared to BDIBD–ACE and BDIBD–DMF. Similarconclusions can be also drawn for keto structures.

Generally, it is known that the intramolecular H-bond between a proton donor and a proton acceptor is the internal driving force for the occurrence of ESIPT. Hence, in order to further reveal the crucial factor related to the original ESIPT process, reduced density gradient (RDG) and atoms in molecules topology analysis (AIM) were performed to verify the influence of protonation on the H-bond strength of the three kinds of molecules (Fig. 3g–l and Table S39, ESI†). The system is mainly based on van der Waals forces, and –O–H···N exists as hydrogen bonding interaction. For BDIBD–DMF, the peak of the discrete plots is located at negative sign($\lambda_2$)$\rho$ with a value of $\sim -0.02$ and the $\delta g$ of the highest discrete plots peak is located at $\sim 0.15$, implying a typical H-bond attraction. It was found that for BDIBD–ACE and BDIBD–MeOH, the discrete plots spikes shifted toward more negative values of sign($\lambda_2$)$\rho$ with certain amounts of deviation, indicating that protonation could greatly enhance the intramolecular H-bond strength and thus facilitate the ESIPT process (BDIBD–DMF < BDIBD–ACE ~ BDIBD–MeOH). In addition, the bond critical point (BCP) generally appears between the attractive atom pair. The value of real space functions at BCP have great significance to analyze the weak interaction. For example, the value of density of all electrons at BCP is closely related to bond strengthening in analogous bond type, and potential energy density at BCP has also been shown to be highly correlated with hydrogen bond energies. Therefore, AIM topology analysis also confirms that the intramolecular H-bond is the strongest with a binding energy of 1.79 and 3.50 kcal $mol^{-1}$,respectively (calculated bond energy, Table S39, ESI†).

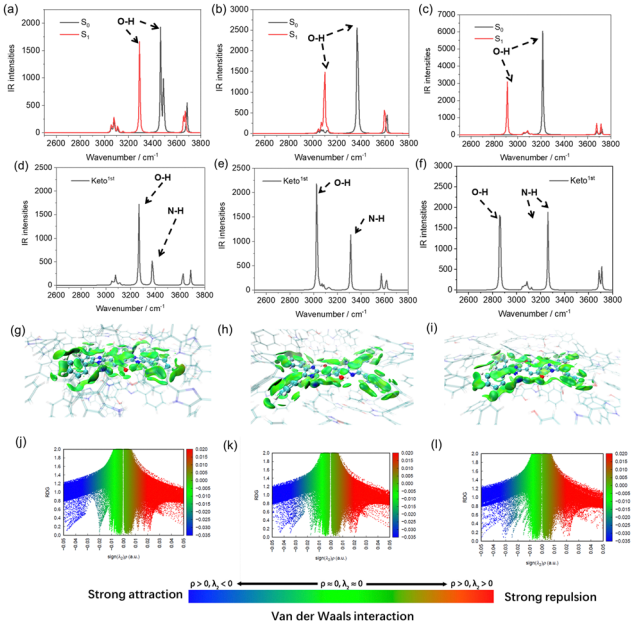


Fig. 3 Simulated IR vibrational spectra of O–H synergetic stretching mode for (a) BDIBD–DMF, (b) BDIBD–ACE and (c) BDIBD–MeOH compounds in both $S_0$ and $S_1$ states. Simulated IR vibrational spectra of O–H and N–H stretching modes formed by proton transfer synergetic stretching for (d) BDIBD–DMF, (e) BDIBD–ACE and (f) BDIBD–MeOH compounds in the $S_1$-keto$^{1st}$ state. Intermolecular interactions in (g) BDIBD–DMF, (h) BDIBD–ACE and (i) BDIBD–MeOH. Reduced density gradient (RDG) scatter plots demonstrating the hydrogen bonding interactions of (j) BDIBD–DMF, (k) BDIBD–ACE and (l) BDIBD–MeOH, with RDG representing the hydrogen bond strength and sign ($\lambda_2$)$\rho$ representing the interaction type by different colors.

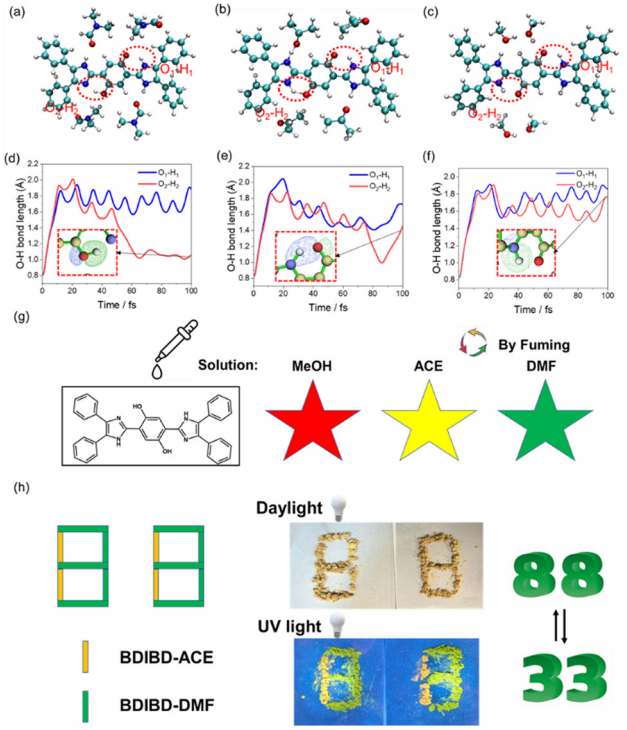


Fig. 4 The chemical structure of (a) BDIBD–DMF, (b) BDIBD–ACE and (c) BDIBD–MeOH at the end of AIMD simulations. The curve of the statistical O–H bond length over time for (d) BDIBD–DMF, (e) BDIBD–ACE and (f) BDIBD–MeOH. Insets: Natural adaptive orbitals (NAdO) around the ESIPT reaction site of the crystals at 100 fs. (g) Left: Chemical structures of BDIBD. Right: Schematic of the multicolor crystal systems and their application in vapor detection. (h) Application of the crystals in information encryption.

To gain insight into the detailed time evolution information on ESIPT crystals, *ab initio* molecular dynamics (AIMD) simulations based on the TD-DFT calculations were conducted to verify the time-scaled proton transfer and the proton transfer ability of the BDIBD molecule (Fig. 4a–f). AIMD was studied for simulated complexes changes in the excited state performed at PBE0/def2-SV(P) with RIJCOSX approximation employing ORCA 5.0.4 package.[45] As is known, the ESIPT progress can be completed within 100 fs. The initial temperature was set at 100 K, the thermal bath temperature was set at 298 K, the calculation time was set at 100 fs, and the step size was set at 0.5 fs. All data analyses as well as the drawing of various visual iso-surfaces or plane maps were obtained by the approach proposed using Multiwfn program and rendered by VMD visualization program. The first ESIPT progress can be easily completed in BDIBD–DMF, but the length of the $O_2$-$H_2$ bond was only ~1 Å at the end of AIMD, showing that the second EISPT progress cannot occur. For BDIBD–MeOH, the lengths of two O–H bonds were ~1.8 Å at the end of AIMD; thus, the two EISPT reactions can both take place. Natural adaptive orbitals (NAdO) were obtained by Multiwfn program, indicating the different delocalization index of the bond in the crystals. Under set conditions, only one proton transfer reaction can occur in BDIBD–DMF, but both two reactions can progress in BDIBD–MeOH. For BDIBD–ACE, as the second proton transfer progress is incomplete, its reactivity is between the other two crystals. The result indicates the different proton transfer ability of the crystals, further confirming the ESIPT intermolecular interaction mechanism.

The above results have shown that the emission of BDIBD-based crystals can be tuned by different solvent-interacting systems, with potential for sensing and light display. As shown in Fig. 4g, BDIBD shows responsiveness to fumigation in the crystal state, which is considered as an ideal method to regulate the multicolor emissions on account of its mild condition. In light of the unique property of BDIBD-based crystals, their potential applications in dynamic multicolor display and information encryption were further investigated. As shown in Fig. 4h, a digital pattern "88" was designed and prepared by BDIBD–ACE and BDIBD–DMF corresponding to the orange and green parts in the designed pattern, respectively. A yellow "88" pattern can be detected under daylight, while the pattern decodes the new information "33", which can be detected under UV light. The part containing information exhibits green emission, while the other part remains yellow color. The crystals have good stability and can be used for long-term storage of information (Fig. S15, ESI†). The above results demonstrated the application potential of BDIBD crystal as a multicolor luminescent material.

## 3. Conclusions

To conclude, synergetic conformational regulations in ground and excited states for realizing modifiable ESIPT emissions were achieved and clearly proved by tuning the intermolecular interactions of a dual-ESIPT site molecule with different crystallizers. By comparing the photophysical properties and comprehensive calculation of the series of crystallizers, it was confirmed that the emission of BDIBD–DMF can come from the first step ESIPT (keto$^{1st}$) excited state, while that of BDIBD–ACE and BDIBD–MeOH is attributable to the second step ESIPT (keto$^{2nd}$) emission. The unique emission tuning properties of the ESIPT chromophores were mainly because of the changes in the ground state of crystal conformations and further intermolecular interactions. In addition, the study of reduced density gradient (RDG) analysis and *ab initio* molecular dynamics (AIMD) simulations specifically proves the different proton transfer ability of dual-ESIPT molecules in the excited states. Based on this, an intrinsic fine regulation system that undergoes different ESIPT processes determined by intermolecular interactions is established for rich luminescent performances. The proposed mechanism provides a theoretical basis for the application of novel optical materials, including efficient displaying, anticounterfeiting, and sensing.

## Data availability

The data are available upon request from the authors.

 

## Conflicts of interest

There are no conflicts to declare.

## Acknowledgements

This work was supported by NKRD Program of China (2021 YFA1500401) and NSFC (22171291, 92261114, 9246130050, 21821003).

## Notes and references

1 L. Chen, P. Y. Fu, H. P. Wang and M. Pan, Excited-state intramolecular proton transfer (ESIPT) for optical sensing in solid state, *Adv. Opt. Mater.*, 2021, **9**, 2001952.
2 V. S. Padalkar and S. Seki, Excited-state intramolecular proton-transfer (ESIPT)-inspired solid state emitters, *Chem. Soc. Rev.*, 2016, **45**, 169–202.
3 J. E. Kwon and S. Y. Park, Advanced organic optoelectronic materials: harnessing excited-state intramolecular proton transfer (ESIPT) process, *Adv. Mater.*, 2011, **23**, 3615–3642.
4 P. Y. Fu, S. Z. Yi, M. Pan and C. Y. Su, Excited-state intramolecular proton transfer (ESIPT) based metal–organic supramolecular optical materials: energy transfer mechanism and luminescence regulation strategy, *Acc. Mater. Res.*, 2023, **4**, 939–952.
5 Y. H. Chen, S. Lu, S. A. A. Abedi, M. Jeong, H. D. Li, M. H. Kim, S. Park, X. G. Liu, J. Y. Yoon and X. Q. Chen, Janus-type ESIPT chromophores with distinctive intramolecular hydrogen-bonding selectivity, *Angew. Chem., Int. Ed.*, 2023, **62**, e202311543.
6 W. Z. Huang, S. Huang, Y. P. Fang, T. Y. Zhu, F. Y. Chu, Q. H. Liu, K. Q. Yu, F. Chen, J. Dong and W. B. Zeng, AI-powered mining of highly customized and superior ESIPT-based fluorescent probes, *Adv. Sci.*, 2024, **11**, 2405596.
7 X. Wang, H. B. Chen, Y. J. Lei, Y. C. Li and B. H. Xiao, Photoconductance induced by excited-state intramolecular proton transfer (ESIPT) in single-molecule junctions, *Adv. Mater.*, 2024, **36**, 2413529.
8 A. C. Sedgwick, L. L. Wu, H. H. Han, S. D. Bull, X. P. He, T. D. James, J. L. Sessler, B. Z. Tang, H. Tian and J. Yoon, Excited-state intramolecular protontransfer (ESIPT) based fluorescence sensors and imaging agents, *Chem. Soc. Rev.*, 2018, **47**, 8842–8880.
9 C. L. Chen, Y. T. Chen, A. P. Demchenko and P. T. Chou, Amino proton donors in excited-state intramolecular proton-transfer reactions, *Nat. Rev. Chem.*, 2018, **2**, 131–143.
10 W. Z. Huang, S. Huang, Y. P. Fang, T. Y. Zhu, F. Y. Chu, Q. H. Liu, K. Q. Yu, F. Chen, J. Dong and W. B. Zeng, AI-powered mining of highly customized and superior ESIPT-based fluorescent probes, *Adv. Sci.*, 2024, 2405596.
11 Y. Wang, H. Y. Mu, Y. H. Sun, J. A. Gao, X. D. Zhu and H. Li, Modulating the ESIPT mechanism and luminescence characteristics of two reversible fluorescent probes by solvent polarity: a novel perspective, *Molecules*, 2024, **29**, 1629.
12 N. J. Yang, G. C. Yue, Y. Zhang, X. Y. Qin, Z. Q. Gao, B. X. Mi, Q. L. Fan and Y. Qian, Reproducible and high-performance WOLEDs based on independent high efficiency triplet harvesting of yellow hot-exciton ESIPT and blue TADF emitters, *Small*, 2024, **20**, 2304615.
13 J. Qiang, Y. R. Wang, Y. J. Li, Z. W. Guo, L. Jiang, F. Wang, S. Lu and X. Q. Chen, A dual-locked near-infrared fluorescent probe based on ESIPT and FRET for improved discrimination between normal and cancer cells, *Sens. Actuators, B*, 2024, **405**, 135344.
14 P. Y. Fu, S. Z. Yi, Z. H. Wang, Y. T. Huang, Y. N. Fan and M. Pan, TADF regulation by tuning keto-energy levels, ISC/RISC equilibrium in coordination polymers with excited state intramolecular proton transfer (ESIPT), *Adv. Opt. Mater.*, 2024, **12**, 2303025.
15 C. Y. Peng, J. Y. Shen, Y. T. Chen, P. J. Wu, W. Y. Hung, W. P. Hu and P. T. Chou, Optically triggered stepwise double-proton transfer in an intramolecular proton relay: a case study of 1,8-dihydroxy-2-naphthaldehyde, *J. Am. Chem. Soc.*, 2015, **137**, 14349–14357.
16 S. Z. Yi, B. N. Li, P. Y. Fu, M. Pan and C. Y. Su, Interplay of dual-proton transfer relay to achieve full-color panel luminescence in excited-state intramolecular proton transfer (ESIPT) fluorophores, *ACS Appl. Mater. Interfaces*, 2023, **15**, 3172–3181.
17 C. C. Yan, Y. P. Liu, W. Y. Yang, J. J. Wu, X. D. Wang and L. S. Liao, Excited state intramolecular proton transfer parent core engineering for six-level system lasing toward 900 nm, *Angew. Chem., Int. Ed.*, 2022, **61**, e202210422.
18 Z. M. Wang, F. Zhou, J. Wang, Z. J. Zhao, A. J. Qin, Z. Q. Yu and B. Z. Tang, Electronic effect on the optical properties and sensing ability of AIEgens with ESIPT process based on salicylaldehyde azine, *Sci. China: Chem.*, 2018, **61**, 76–87.
19 C. H. Wang, Z. Y. Liu, C. H. Huang, C. T. Chen, F. Y. Meng, Y. C. Liao, Y. H. Liu, C. C. Chang, E. Y. Li and P. T. Chou, Chapter open for the excited-state intramolecular thiol proton transfer in the room-temperature solution, *J. Am. Chem. Soc.*, 2021, **143**, 12715–12724.
20 V. P. Rahane, A. Shukla, R. B. Roseli, A. R. Ireland, I. Gale, E. H. Krenske, E. G. Moore, E. B. Namdas, N. Jain and S. C. Lo, Low amplified spontaneous emission threshold from solution processable excited-state intramolecular proton transfer chromophores, *Adv. Opt. Mater.*, 2024, 2400840.
21 M. Chen, X. Y. Chen, Y. Wang, X. H. Fan, T. S. Chen and Z. H. Liang, An ESIPT fluorescent probe for ultrarapid HClO detection during reagent-stimulated oxidative stress in cells and zebrafish, *Sens. Actuators, B*, 2022, **371**, 132545.
22 T. He, N. Niu, Z. J. Chen, S. J. Li, S. X. Liu and J. Li, Novel quercetin aggregation-induced emission luminogen (AIEgen) with excited-state intramolecular proton transfer for in vivo bioimaging, *Adv. Funct. Mater.*, 2018, **28**, 1706196.
23 K. C. Tang, M. J. Chang, T. Y. Lin, H. A. Pan, T. C. Fang, K. Y. Chen, W. Y. Hung, Y. H. Hsu and P. T. Chou, Fine tuning the energetics of excited-state intramolecular proton transfer (ESIPT): white light generation in a single ESIPT system, *J. Am. Chem. Soc.*, 2011, **133**, 17738–17745.

24 J. K. Wang, C. H. Wang, C. C. Wu, K. H. Chang, C. H. Wang, Y. H. Liu, C. T. Chen and P. T. Chou, Hydrogen-bonded thiol undergoes unconventional excited state intramolecular proton-transfer reactions, *J. Am. Chem. Soc.*, 2024, **146**, 3125–3135.
25 F. Arenhart Soares, G. Martinez-Denegri, L. A. Baptista, P. Sleczkowski and A. Steinbüchel, Balancing the push–pull effect on the synthesis and fluorescent properties of new ESIPT dyes for thin film applications, *J. Phys. Chem. C*, 2023, **127**, 17624–17636.
26 J. F. Berbigier, L. G. T. A. Duarte, J. M. Perez, R. A. Mendes, E. Zapp, T. D. Z. Atvars, A. G. Dal-Bó and F. S. Rodembusch, Excited state intramolecular proton transfer process in benzazole fluorophores tailored by polymeric matrix: a combined theoretical and experimental study, *J. Mol. Liq.*, 2019, **295**, 111710.
27 S. H. Hwang, H. Kim, H. Ryu, I. E. Serdiuk, D. Lee and T. L. Choi, Powerful direct C-H amidation polymerization affords single-fluorophore-based white-light emitting polysulfonamides by fine-tuning hydrogen bonds, *J. Am. Chem. Soc.*, 2022, **144**, 1778–1785.
28 F. Joy, K. P. Chaithra, A. Nizam, A. Deepti, P. S. B. Chakrapani, A. K. Das, T. P. Vinod and Y. Nair, A multi-stimuli responsive organic luminogen with aggregation induced emission for the selective detection of Zn2+ ions in solution and solid state, *Chem. Eng. J.*, 2023, **453**, 139798.
29 K. L. Wu, T. Zhang, Z. A. Wang, L. Wang, L. S. Zhan, S. L. Gong, C. Zhong, Z. H. Lu, S. Zhang and C. L. Yang, De novo design of excited-state intramolecular proton transfer emitters via a thermally activated delayed fluorescence channel, *J. Am. Chem. Soc.*, 2018, **140**, 8877–8886.
30 W. Yin, Y. Li, N. Li, W. Y. Yang, H. An, J. R. Gao, Y. Bi and N. Zhao, Hybridization of triphenylamine and salicylaldehyde: a facile strategy to construct aggregation-induced emission luminogens with excited-state intramolecular proton transfer for specific lipid droplets and Gram-positive bacteria imaging, *Adv. Opt. Mater.*, 2020, **8**, 1902027.
31 M. Z. Chen, H. Hu, X. Cheng, Y. Wu, Z. M. Ma, R. P. Sijbesma and Z. Y. Ma, Multicolor polymer mechanochromism from an ultrasensitive concentration dependent excited state intramolecular proton transfer mechanophore, *Adv. Opt. Mater.*, 2024, 2400733.
32 Y. P. Li, X. H. Zhu, S. N. Li, Y. C. Jiang, M. C. Hu and Q. G. Zhai, Highly selective and sensitive turn-off–on fluorescent probes for sensing Al ions designed by regulating the excited-state intramolecular proton transfer process in metal–organic frameworks, *ACS Appl. Mater. Interfaces*, 2019, **11**, 11338–11348.
33 J. D. Wang, F. J. Huo, Y. B. Zhang and C. X. Yin, Spiropyran isomerization triggering ESIPT for visualization of pH fluctuations during oxidative stress in living cells, *Chin. Chem. Lett.*, 2023, **34**, 107818.
34 M. Frisch, G. W. Trucks, J. Schlegel, G. E. Scuseria, M. A. Robb, J. R. Cheeseman, H. B. Schlegel, G. Scalmani, V. Barone, B. Mennucci and G. A. Petersson, *Gaussian 09, Revision C.01*, Gaussian, Inc, Wallingford, CT, 2009.
35 T. Lu and F. Chen, Multiwfn: a multifunctional wavefunction analyzer, *J. Comput. Chem.*, 2012, **33**, 580–592.
36 Z. Y. Liu, T. Lu and Q. X. Chen, An sp-hybridized all-carboatomic ring, cyclo[18]carbon: Electronic structure, electronic spectrum, and optical nonlinearity, *Carbon*, 2020, **165**, 461–467.
37 W. Humphrey, A. Dalke and K. Schulten, VMD: visual molecular dynamics, *J. Mol. Graphics*, 1996, **14**(33–38), 27–28.
38 B. F. Cao, J. H. Han, Q. Zhou, C. F. Sun, Y. Li, B. Li, H. Yin and Y. Shi, Skillfully tuning 1-hydroxy-9H-fluoren-9-one forward-backward ESIPT processes by introducing electron-withdrawing groups: A theoretical exploration, *J. Mol. Liq.*, 2020, **303**, 112627.
39 L. G. T. A. Duarte, E. S. Moraes, P. S. S. Wakabayashi, L. C. da Luz, R. Cercená, E. Zapp, T. D. Z. Atvars, A. G. Dal-Bó and F. S. Rodembusch, Revealing the ESIPT process in benzoxazole fluorophores within polymeric matrices through theory and experiment, *Photochem. Photobio.*, 2024, DOI: **10.1111/php.13991**.
40 J. J. Hao and Y. Yang, Unveiling the effect of solvent polarity on the excited state intramolecular proton transfer mechanism of new 3-hydroxy-4-pyridylisoquinoline compound, *Spectrochim. Acta, Part A*, 2020, **232**, 118082.
41 C. Z. Li, B. Hu and Y. F. Liu, Unraveling the effect of two different polar solvents on the excited-state intramolecular proton transfer of 4'-methoxy-3-hydroxyflavone fluorescent dye, *Spectrochim. Acta, Part A*, 2020, **225**, 117487.
42 M. Ma, Y. J. Zhang and C. F. Sun, Regulating the ESIPT processes and photophysical properties of indole derivates by introducing the appropriate functional groups, *J. Mol. Liq.*, 2023, **384**, 122263.
43 A. I. Skilitsi, D. Agathangelou, I. Shulov, J. Conyard, S. Haacke, Y. Mély, A. Klymchenko and J. Léonard, Ultrafast photophysics of the environment-sensitive 4-methoxy-3-hydroxyflavone fluorescent dye, *Phys. Chem. Chem. Phys.*, 2018, **20**, 7885–7895.
44 Y. F. Yang, Y. Ding, W. Shi, F. C. Ma and Y. Q. Li, The effects of amino group meta- and para-substitution on ESIPT mechanisms of amino 2-(2'-hydroxyphenyl) benzazole derivatives, *J. Lumin.*, 2020, **218**, 116836.
45 F. Neese, Software Update: The ORCA Program System, Version 4.0, *WIREs Comput. Mol. Sci.*, 2018, **8**, e1327.

 